ORCHYD

"Novel Drilling Technology Combining Hydro-Jet and Percussion for ROP Improvement in deep geothermal drilling"

HORIZON 2020
THE FRAMEWORK PROGRAMME FOR RESEARCH AND INNOVATION

This project has received funding from the European Union's Horizon 2020 research and innovation programme under grant agreement No 101006752

DELIVERABLE D5.2

"Report on modelling, prediction and feasibility of the intensifier when using drilling vibrations or fluid drilling energy"

ABSTRACT

To demonstrate the potential of the new drilling technique targeted by ORCHYD, it is essential to assess the performance of different intensifier design and operating parameters. Therefore, the main objective of this report is to provide a parametric study with graphic illustration of the HPWJ performance with different intensifier designs starting with drill-string vibration. This report is covers: (1) numerical simulation of the intensifier utilizing axial vibration energy of the drill string; (2) working description of the intensifier utilizing axial vibration energy of the drill string; (3) numerical simulation of nozzle with different chamber pressure; (4) factors influencing the failure mechanisms of ultra-high pressure water jets cutting rock under atmospheric pressure with submerged condition.

The main results show that the chamber pressure is greatly affected by the structural parameters and working parameters of the intensifier, and the maximum pressure is about 150 MPa. The length of the potential core of the jet is about 7 times the diameter of the nozzle. The grooves formed by ultra-high pressure jet slotting mainly have either a long regular shape or a funnel shape. In the case of small stand-off distance and ultra-high pressure, regular grooving occurs. In the case of large stand-off distance, block spalling is the main reason for irregular changes of rock breaking volume with jet traversing distance.

A very important outcome of this research for the ORCHYD project is the understanding of the influence of WOB and vibration frequency. It was confirmed from Drillstar that the percussive mud-hammer's effective operational range uses a small WOB and high frequency and that this will yield insufficient energy to activate a vibrational intensifier that could produce the targeted 150 MPa. Intensifier design has switched to focus on other technologies (such as screw type intensifiers).

Disclaimer

The present document reflects only the author's view. The European Innovation and Networks Executive Agency (INEA) is not responsible for any use that may be made of the information it contains.

DOCUMENT TYPE	Deliverable
DOCUMENT NAME:	D5.2 - Report on modelling, prediction and feasibility of the intensifier when using drilling vibrations or fluid drilling energy
VERSION:	vfinal
DATE:	29/06/2022
STATUS:	S0
DISSEMINATION LEVEL:	PU

AUTHORS, REVIEWERS				
AUTHOR(S):	Huajian Wang			
AFFILIATION(S):	China University of Petroleum (UPC)			
FURTHER AUTHORS:	Hualin Liao;Yongwang Liu; Jinkai Chen; Jian Zhao; Jun Wei			
PEER REVIEWERS:	John Paul Latham, Hedi Sellami			
REVIEW APPROVAL:	Approved	Yes	Rejected (to be improved as indicated below)	
REMARKS / IMPROVEMENTS:				

VERSION HISTORY				
VERSION:	DATE:	COMMENTS, changes, STATUS:		PERSON(S) / ORGANISATION SHORT NAME:
v0.1	18/05/2022	Draft before peer-review approval		Huajian Wang (UPC)
v1.1	17/06/2022	After the first review		John Paul Latham (ICL)，Hedi Sellami（ARMINES）
v2.1	22/06/2022	After the second review		John Paul Latham (ICL)，Hedi Sellami（ARMINES）
vfinal	29/06/2022	Deliverable ready to be submitted		Hualin Liao (UPC)

VERSION NUMBERING	
v0.x	Draft before peer-review approval
v1.x	After the first review
v2.x	After the second review
vfinal	Deliverable ready to be submitted!

STATUS / DISSEMINATION LEVEL			
STATUS		DISSEMINATION LEVEL	
S0	Approved/Released/Ready to be submitted	PU	Public
S1	Reviewed	CO	Confidential, restricted under conditions set out in the Grant Agreement.
S2	Pending for review		
S3	Draft for comments	CI	Classified, information as referred to in Commission Decision 2001/844/EC.
S4	Under preparation		

TABLE OF CONTENTS

CONTENT

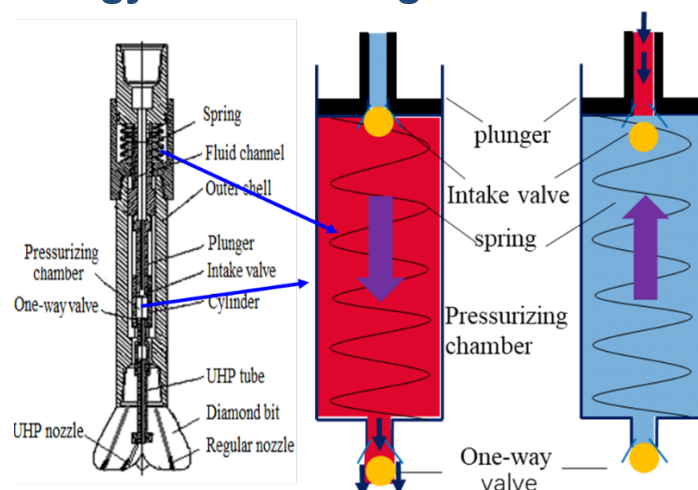# 1 Working description of intensifier utilizing axial vibration energy of drill string

Fig.1. Vibration reduction and pressurization system

By investigating the motions of rotary drill strings in wellbore, including rotation, axial and lateral vibrations, and so forth, researchers proposed that the energy of the axial vibration can be used as a downhole pressurizing method. As is shown in Fig.1, the intensifier utilizes the axial vibration energy of drill strings, as a substitute of the fluid energy, to drive the plunger. This energy-saving mode not only diminishes the amplitude of the vibration by energy absorption, but pressurizes the fluid to an ultra-high level as an auxiliary power to break the rock[1-3].

During the down stroke, when the axial downward vibration load of the drill string exceeds the pre-tightening force of the spring, it compresses the spring and drives the plunger forward, as the intake valve inside the plunger now is in a closed state, hence the fluid inside the cylinder can be pressurized. Once the fluid pressure surpasses the critical value of the one-way valve, which consequently opens, the pressurized fluid can eject through UHP nozzles to cut the rock.

In the upstroke, due to the combined effect of the vibration and the spring, the plunger goes upward with the drill string. The pressure difference thus generated shuts the one-way valve and opens the intake valve, allowing the fluid flow into the cylinder. The reciprocating motion driven by the vibration energy of the drill strings, in this way, continuously generates high pressure fluid flow to assist the drill bit to break the rock, increasing the rate of penetration (ROP).

2 Numerical simulation of the intensifier utilizing axial vibration energy of drill string
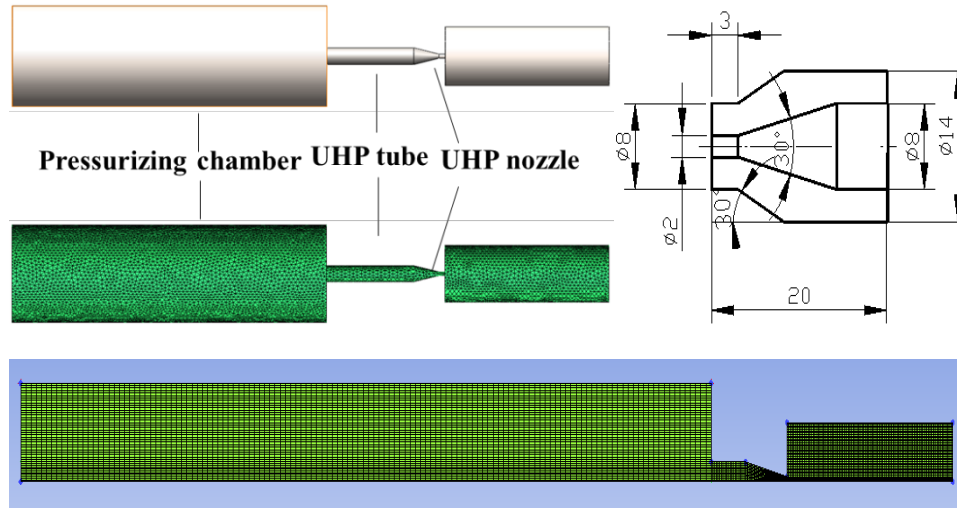
2.1 Structural parameters

Fig.2. Structure of chamber and nozzle

The assembly of the vibration reduction and pressurization system is shown in Fig.2. The pressurization components are simplified and the fluid simulation physical model is as shown in Fig.2. The specific structural parameters are shown in Table 1.

Table 1. Structure parameters of chamber and nozzle

structure	parameter	value	unit
Pressurizing chamber	Diameter of chamber	40-55	mm
	Length of chamber	200	mm
	Diameter of UHP tube	8	mm
	Length of UHP tube	10	mm
nozzle	Diameter of inlet	8	mm
	Diameter of outlet	2	mm
	Length	20	mm
	Angle of convergence	30	°

2.2 Parameters of numerical simulation

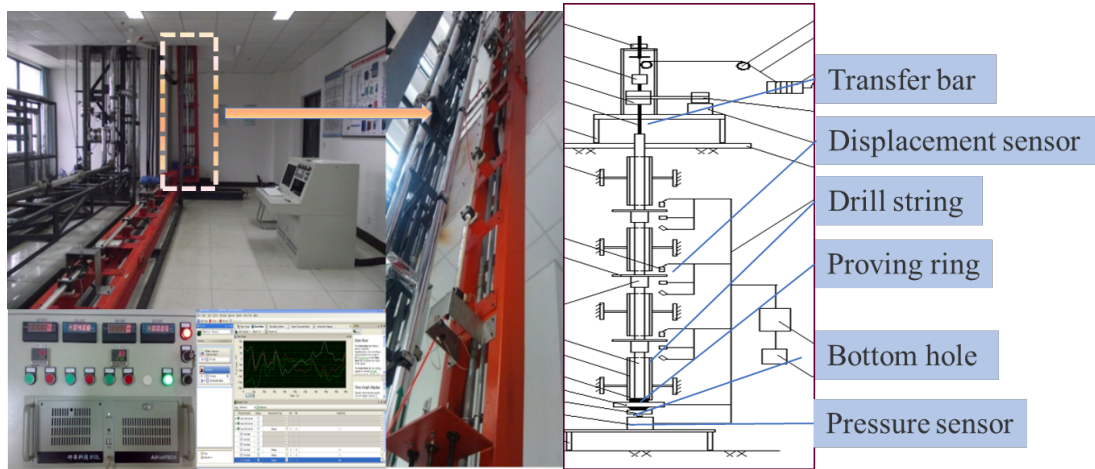### 2.2.1 The longitudinal vibration experimental device


Fig.3.Vibration test system

The drillstring dynamic simulation experimental system was established to study the longitudinal vibration characteristics of the fluctuation law of bottomhole weight on bit (WoB). The vibration test system is as shown in Fig.3. The apparatus is 311mm bit + 228.6mm drill collar x 6 + 203.2mm drill collar x 6 + 127mm drill string.

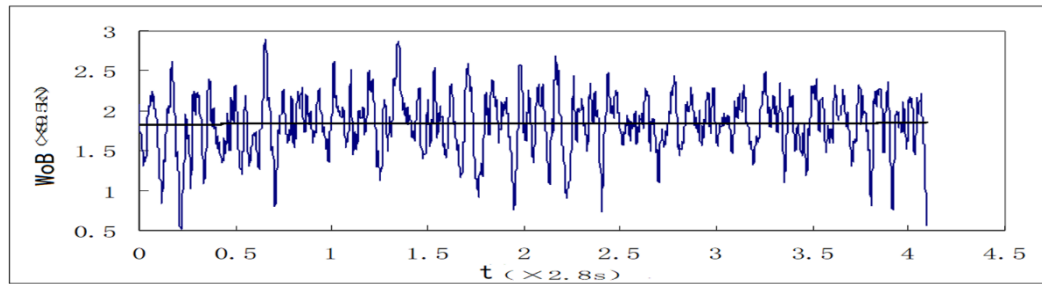### 2.2.2 Vibration characteristics of drill string

Pendulum drilling tool (Fig.4(a).): 311.2 mm hole, 228.6 mm drill collar; rotating speed 69.0 r / min, nominal WOB 178.9 kN. The average WOB is 179.3 kN. When the confidence interval is 90%, the fluctuation range of WOB is 136.1-220.3 kN. When the confidence interval is 80%, the fluctuation range of WOB is 145.2-211.1 kN. The frequency of WOB fluctuation is about three to four times that of rotary speed.

Pendulum drilling tool (Fig.4(b).): 311.2mm hole, 228.6 mm drill collar; rotational speed 92.0 r/min, nominal WOB 178.9kN. The average WOB is 168.5 kN. When the confidence interval is 90%, the fluctuation range of WOB is 105.0-210.4 kN. When the confidence interval is 80%, the fluctuation range of WOB is 123.1-210.2 kN. The frequency of WOB fluctuation is about three to four times that of rotary speed.

Pendulum drilling tool (Fig.4(c).): 311.1mm hole, 228.6mm drill collar; rotating speed 115.0 r/min, nominal WOB 178.9 kN. The average WOB is 160.3 kN. When the confidence interval is 90%, the fluctuation range of WOB is 80.1-236.8 kN. When the confidence interval is 80%, the fluctuation range of WOB is 101.2 ~ 218.5 kN. The frequency of WOB fluctuation is about three to four times that of rotary speed.
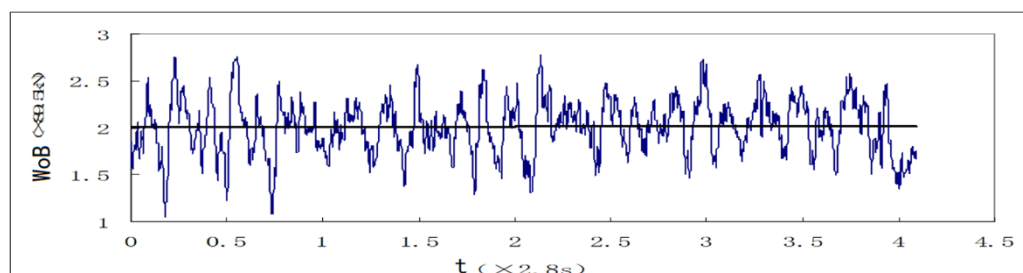
(a) Rotating speed 69.0 r / min

(b) Rotating speed 92.0 r / min
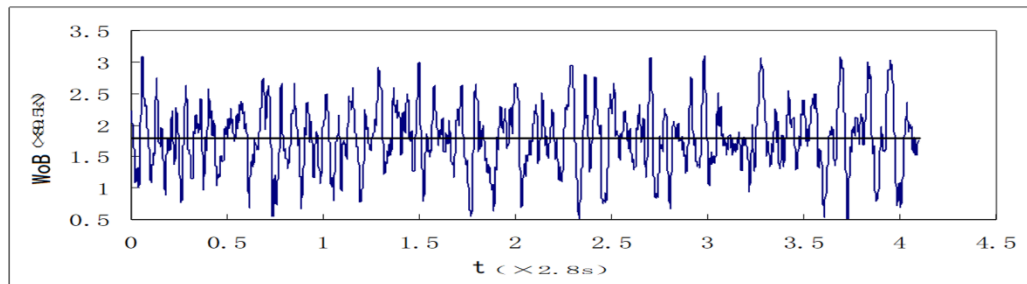
(c) Rotating speed 115.0 r / min

Fig. 4 Vibration characteristic of drill string

According to the vibration characteristic (Fig.3.) of the measured longitudinal vibration signal of the drill string, the longitudinal vibration frequency of the drill string is 3~4 Hz, and the measured frequency spectrum vibration characteristic is similar to a sinusoidal distribution. Therefore, the applied characteristic of WOB is defined as:

$$F_N = F_b + F_{b1} \sin(2\pi f t)$$

(1)

Where F_N is WOB, kN; F_b is average WOB, kN; F_{b1} is pulsating peak WOB, kN; f is frequency of vibration, Hz; t is time, s.
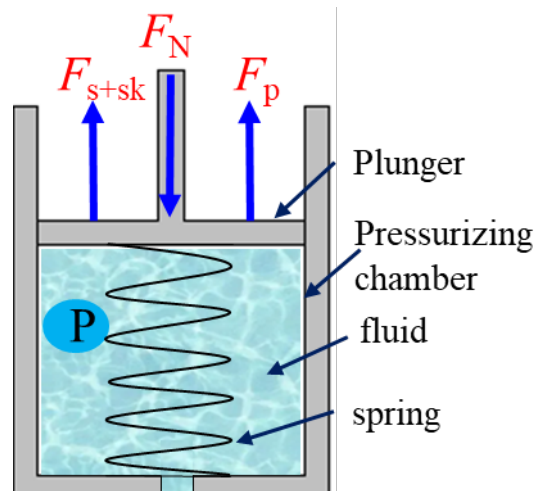
2.2.3 Force of plunger

Fig. 5 Force of plunger

In the process of downward movement, the energy loss of fluid and spring is ignored, and the plunger is mainly acted on by three forces (Fig.5.), F_N is the WOB; F_p is the force of pressure on the plunger; F_{s+sk} is the spring force, which is mainly caused by the precompression force of the spring and the reaction force caused by the compression deformation of the spring in the process of down stroke. We can shorten it to the following expression：

$$F_{s+s_k} = k \cdot (s + s_k)$$

(2)

$$F_p = p \cdot \frac{\pi D^2}{4}$$

(3)

Where k is spring stiffness，N/mm；s_k is the amount of spring precompression，mm；s is the stroke of plunger, mm；p is fluid pressure of chamber, pa，D is diameter of plunger, mm. The resultant of all the external forces is as follows,

$$F_1 = F_N - F_{s+sk} - F_p$$

(4)

2.2.4 Method of numerical simulation

Table 2. Simulation parameters

Parameter	Symbol	Value	Unit
Spring stiffness	k	2500-4000	N/mm
Average WOB	F_b	150	kN
Peak	F_{b1}	50	kN
Frequency	f	2-6	Hz
Spring precompression	s_k	0-80	kN
Diameter of plunger	D	40-55	mm

The jet features with different parameters were studied based on computational fluid dynamics (CFD) using the commercial code FLUENT. In the simulation process, it is assumed that the pressurization chamber is filled with liquid, and the velocity of the liquid in the initial position is 0. The plunger movement process is realized through the moving grid, and the turbulence model is named here the Standard model, while various alternative turbulence models are investigated in Section 3. The liquid in the pressurized chamber was clear water, and the entrance was set as rigid body in the process of setting boundary conditions. The chamber wall surface is set to deforming. The ultra-high pressure flow channel and the nozzle are set as a wall. The fluid domain at the nozzle is set as a pressure-outlet, and the pressure is the gauge pressure. The solution type is pressure based and transient. Specific parameter settings are shown in Table 2.

2.3 Results of numerical simulation

When k is 2500 N/mm; Fb is 150 kN; Fb1 is 50 kN; sk is 0 mm, the results are as follows:

2.3.1 Forming process of UHP water jet

Fig.6. and Fig.7. show the jet forming process and velocity of the UHP water jet. As we can see from these figures, the velocity in the nozzle presents periodic changes, with a period of 0.23 s. The growth process of velocity and the decline process are not completely

symmetrical. Under the above simulated conditions, the peak velocity is 510 m/s (potential core of jet).
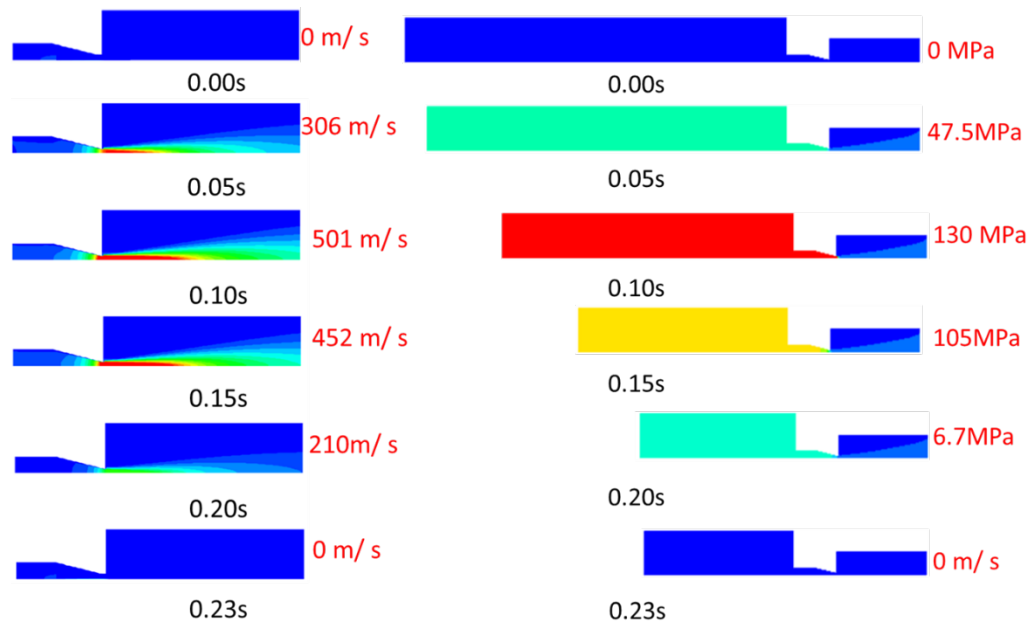

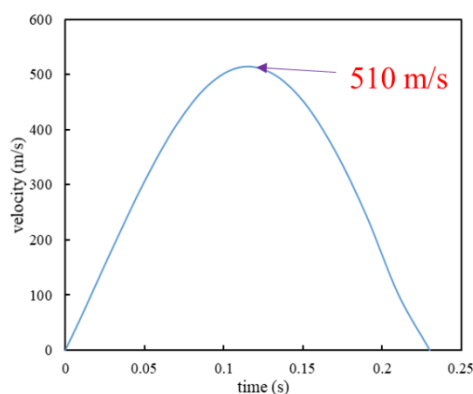Fig.6. Outlet Velocity contour (left) and chamber pressure (right) with time
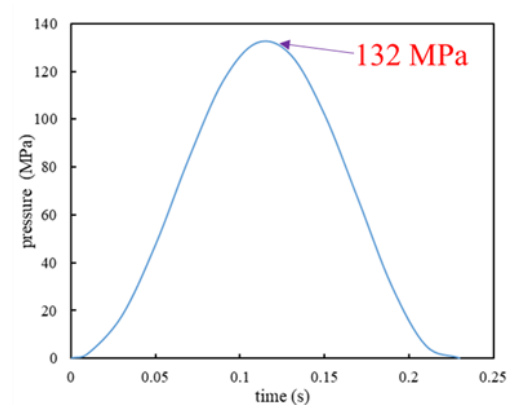

Fig.7. Velocity of UHP water jet   Fig.7. Pressure characteristic in chamber

As we can see from Fig.7, the pressure characteristic in the chamber also presents periodic changes, with a period of 0.23 s. The pressure and velocity have similar characteristics. The pressure peak value (132 MPa) appears at 0.12 s. The pressure-time distribution is similar to gaussian with a growth rate higher at 0.03 s to 0.1 s, and showing linear growth characteristics. The pressure is relatively constant between 0.1 s - 0.15 s, and the pressure value is above 100 MPa. After 0.12 s, the pressure shows a declining trend and the pressure decline rate is higher at 0.14 s - 0.2 s. The pressure gradually drops to 0 MPa at about 0.23 s.

2.3.2 Pressure and velocity characteristics of the flow field
(1) Spring stiffness

(a) Pressure characteristic in chamber   (b) Velocity characteristic in nozzle
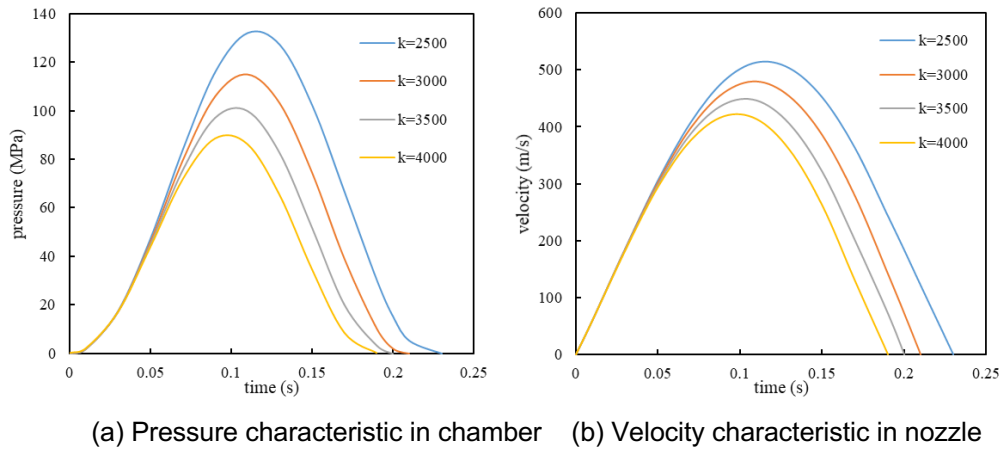
Fig. 8 Characteristics of flow field with different spring stiffness

Fig.8. shows the characteristic of flow field with different spring stiffness. With the increase of spring stiffness, the velocity in nozzle and pressure in chamber are declining significantly. When k is 2500 N/mm, the peak value of pressure and velocity are 132 MPa and 510 m/s respectively, while k is 4000 N/mm, the peak value of pressure and velocity are 90 MPa and 408 m/s respectively. With the increase of k, the period is reduced, when the k is 2500 N/mm, the period is 0.23 s, while k is 4000 N/mm, the period is reduced to 0.19 s.

(2) Frequency of drill string vibration

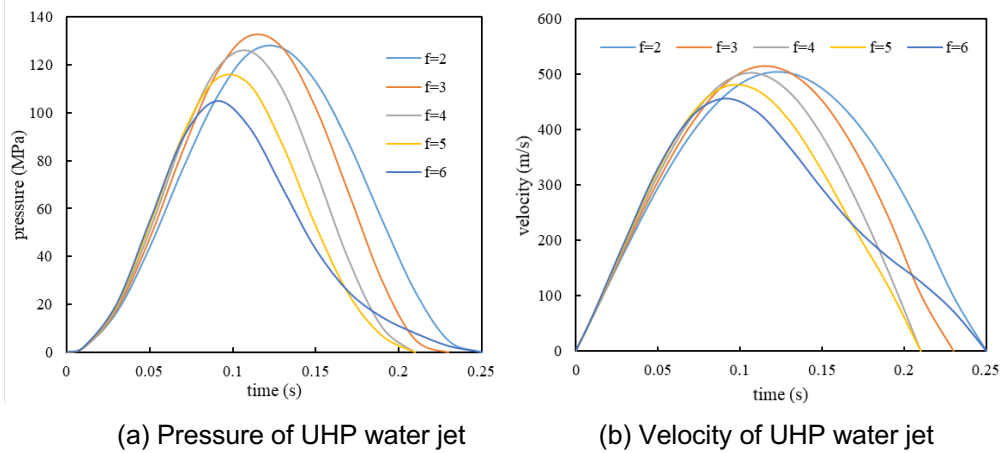(a) Pressure of UHP water jet   (b) Velocity of UHP water jet

Fig.9. Characteristic of flow field in different frequency

Fig.9. shows the characteristic of flow field in different frequency. As we can see from this figure, the increase in frequency reduces the peak value of pressure and velocity, but increases the growth rate of velocity and pressure in general. The reason for this phenomenon is that the increase in frequency results in a rapid increase in WOB, and increases the plunger's downward velocity, while the rapid reduction of the WOB in a short time reduces the acceleration of the plunger, thus shifting the position of peak to the right and reducing the peak value. But when the frequency f is 3 Hz the intensifier has a better pressurization effect, because the natural frequency and vibration frequency of the intensifier are similar, and the pressurizing capability is better (the natural frequency is 3 Hz, the natural frequency depend

on the hardness，mass，overall dimension stiffness and so on, but in this report the natural frequency depend on the stiffness). In general, the lower the frequency, the longer the duration of the high-pressure water jet will be.

(3) Diameter of plunger

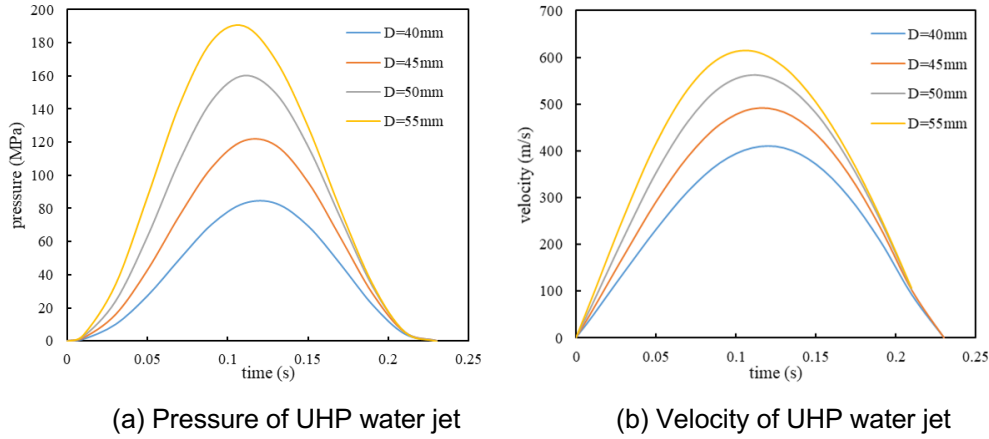| (a) Pressure of UHP water jet | (b) Velocity of UHP water jet |

Fig.10. Characteristic of flow field in different diameter of plunger

In order to study the influence of plunger diameter on the pressurization effect, plunger diameters of 40, 45, 50, 55 and 60 mm were selected. As we can see from Fig.10. The increase of the plunger diameter increases the peak pressure and velocity, reduces the formation time of the ultra-high pressure jet, and increases the time range of the ultra-high pressure water jet. In other words, the increase of the plunger diameter lengthens the holding time of the UHP water jet. And with the increase of diameter of plunger the pressure and velocity increase more rapidly. In the range of diameters investigated, the larger plunger diameter is beneficial to the formation of ultra-high pressure water jet.

（4）Weight on Bit, WOB

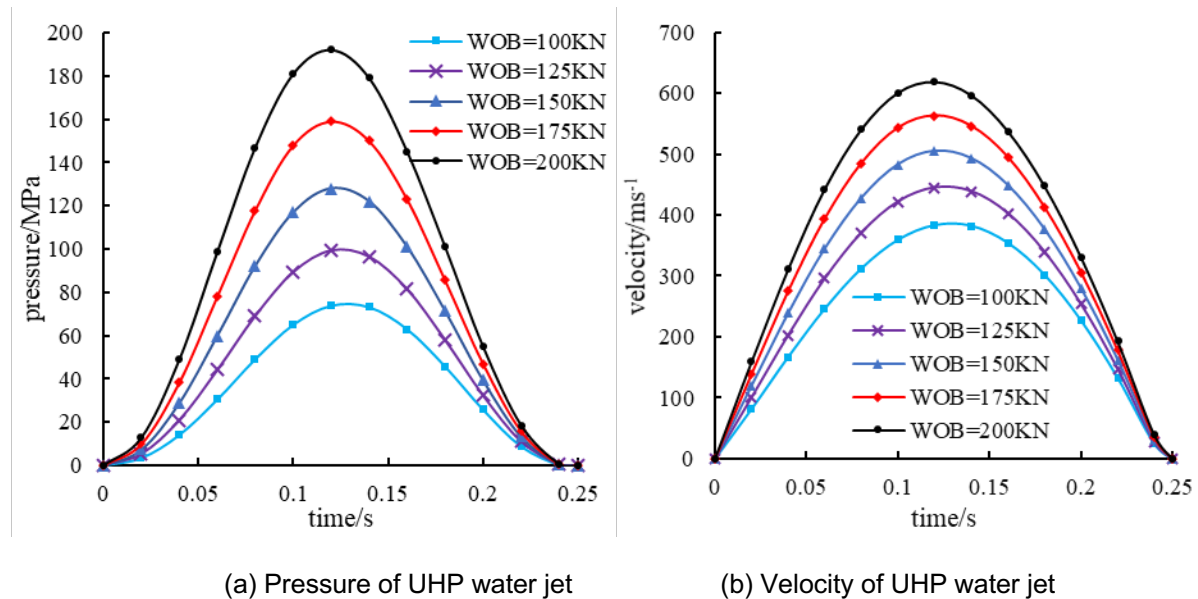| (a) Pressure of UHP water jet | (b) Velocity of UHP water jet |

Fig.11 Characteristic of flow field with different WOB

Fig.11 shows the characteristic of flow field in different WOB. As we can see from this picture, the increase in WOB increase the peak value of pressure and velocity, and increases the growth rate of velocity and pressure in general. The reason for this phenomenon is that the increase in WOB results in a rapid increase in force on the plunger, and increases the plunger's downward velocity. Furthermore, the increase of the WOB increases the time range of the ultra-high pressure water jet, in other words, the increase of the WOB lengthens the holding time of the UHP water jet. In the range investigated, the larger WOB is beneficial to the formation of ultra-high pressure water jet, it was confirmed that for effective ROP with DTH Mud-Hammer, the WOB is much lower (about 50kN) than the range reported here. The WOB does not affect the plunger motion frequency.

（5）**The effect of nozzle diameter**

(a) Pressure of UHP water jet   (b) Velocity of UHP water jet
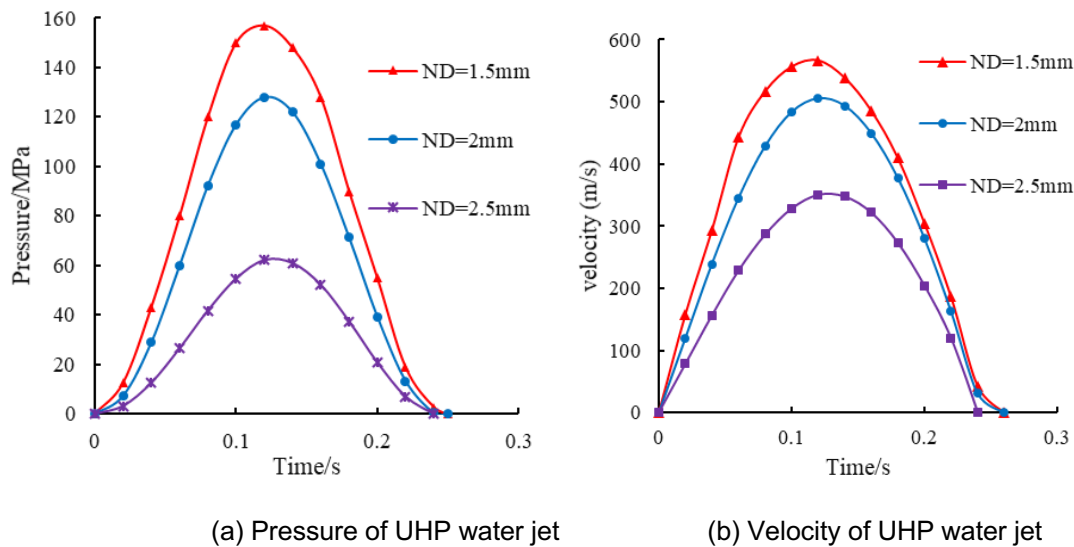
Fig.12 Characteristic of flow field in different nozzle diameter

Fig.12 compares the pressurization effect with different nozzle diameter. It is worth noting that, as the nozzle diameter increases, the peak pressure and velocity increase, and the formation time of the high-pressure water jet is reduced. Increasing the nozzle diameter prolongs the holding time of the high-pressure water jet above a certain threshold value, and the increase of nozzle diameter makes the pressurization period decrease, and with the decrease of nozzle diameter the pressure and velocity increase more rapidly. In the range of diameters investigated in this research, the smaller nozzle diameter is beneficial to the formation of an ultra-high-pressure water jet.

2.3.3 Motion characteristics of plunger
(1) Spring stiffness

(a) Acceleration of plunger

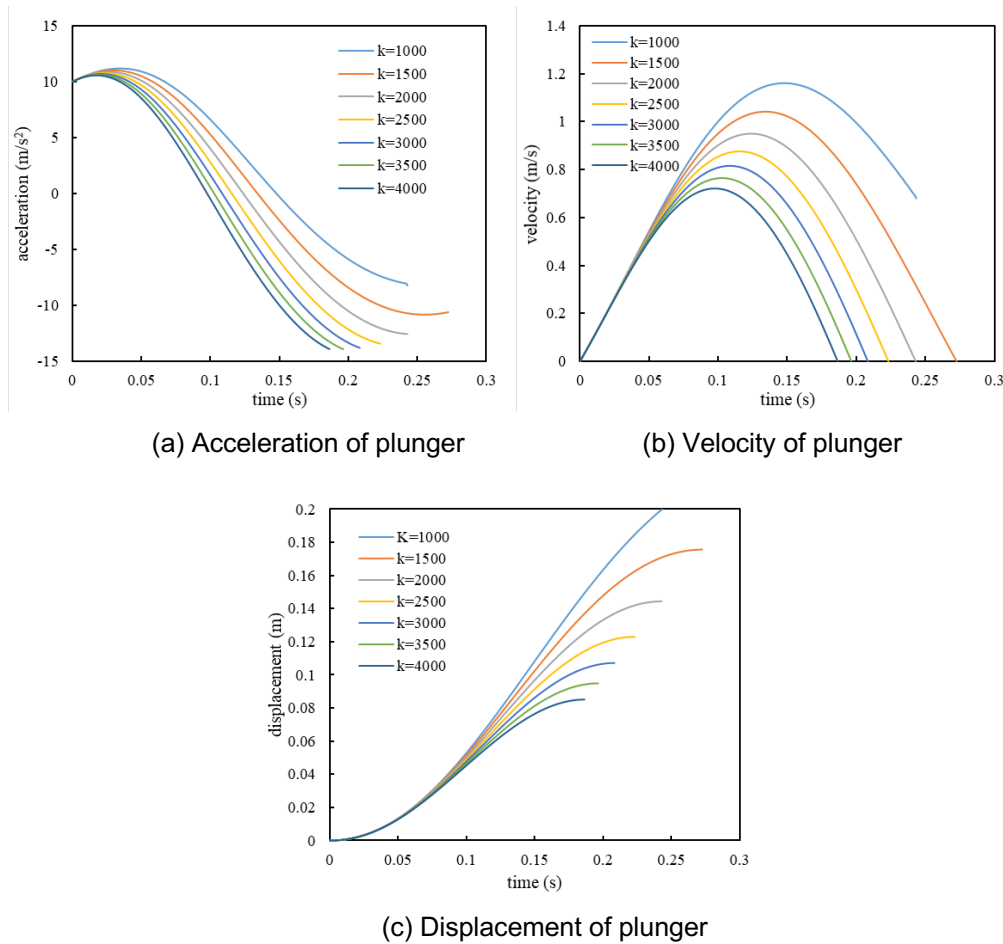(b) Velocity of plunger

(c) Displacement of plunger

Fig.13 Plunger motion characteristics in different spring stiffness

Fig.13 shows the plunger motion characteristics in different spring stiffness, with the increase of spring stiffness, the period of motion of plunger is decreased, and with the greater of spring stiffness, the degree of period reduction decreases in general, but when k is 1000 N/mm, the period is shouter than k=1500 N/mm and k=2000 N/mm, the reason for this phenomenon is that when k is 1000 N/mm the stroke of plunger is bigger than 200 mm, thus causes the plunger velocity to rapidly decrease to 0. The smaller spring stiffness can increase the speed of the plunger and make the pressure rise faster but increase the stroke and may cause the failure of the disc spring.

(2) Frequency of drill string vibration

(a) Acceleration of plunger

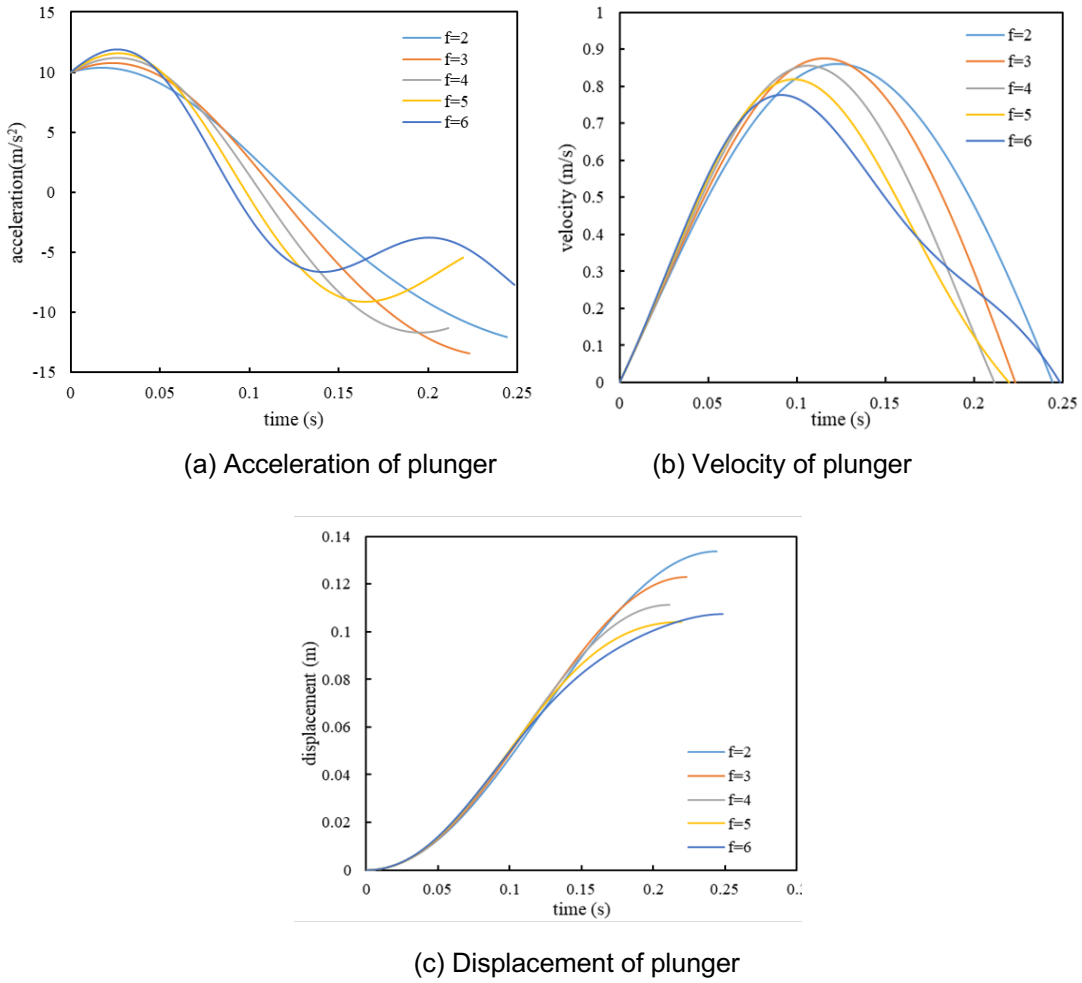(b) Velocity of plunger

(c) Displacement of plunger

Fig.14 Plunger motion characteristics in different frequency

As we can see from Fig.14 the vibration frequency can significantly affect the motion characteristics of plunger and thus affect the pressurization process, the acceleration of the plunger increases first and then decreases, and this phenomenon is more obvious with the increase of the vibration frequency of the drill string, however, when the frequency is greater than 4 Hz, the acceleration decreases, which is caused by the decrease of the WOB. When the vibration frequency is less than 4 Hz, the plunger motion period decreases with the increase of vibration frequency, while the vibration frequency is more than 4 Hz, the plunger motion period increases with the increase of vibration frequency. In terms of displacement, the smaller the vibration frequency, the bigger the displacement of the plunger.

(3) Diameter of plunger

Fig.15 shows the plunger motion characteristics in different diameter of plunger, the overall acceleration showed a trend of first increase and then decrease. Before 0.15 s, the larger the diameter of the plunger, the more obvious the acceleration decreased. After 0.15 s, the opposite trend was presented, that is, the larger the diameter of the plunger, the acceleration gradually decreased. This phenomenon resulted in the trend that the plunger velocity gradually decreased with the increase of the diameter of the plunger, and the plunger diameter does not affect the plunger motion frequency. In terms of displacement, the increase

in plunger diameter reduces stroke of plunger, and with the increase of plunger diameter, the increase degree of plunger displacement becomes larger.
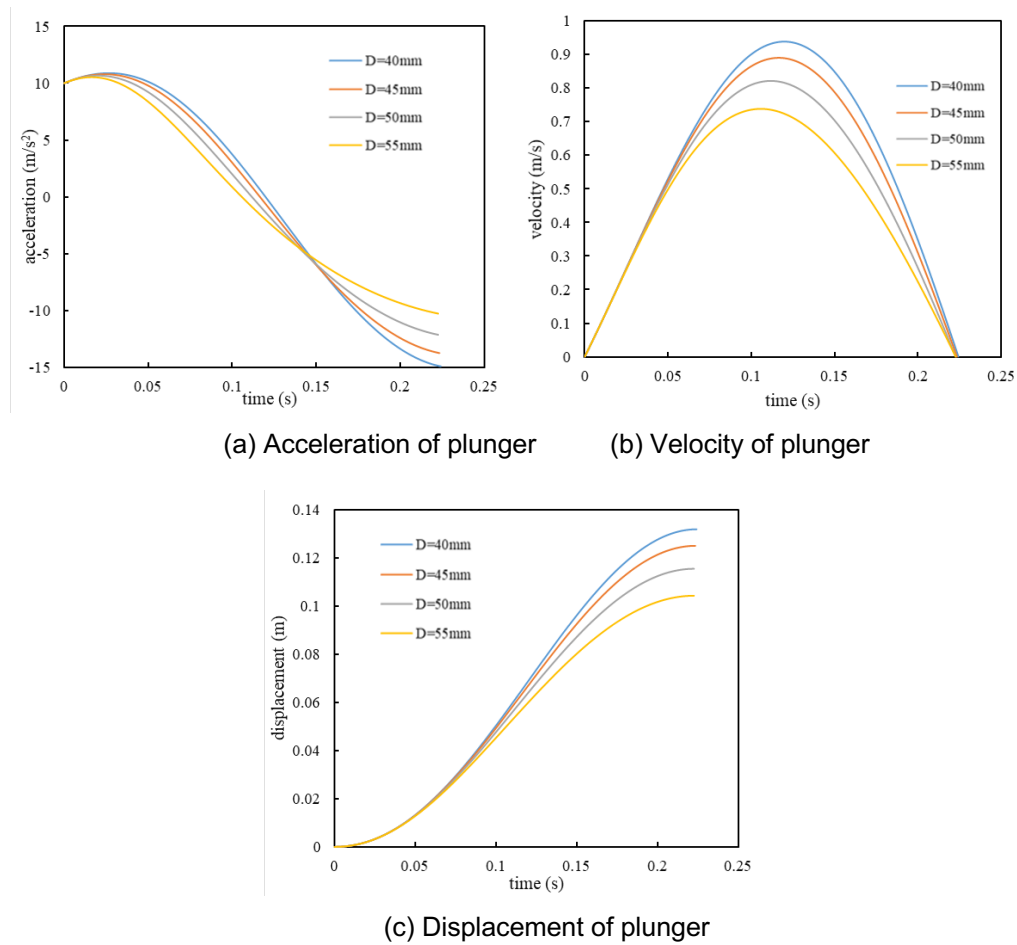

(a) Acceleration of plunger

(b) Velocity of plunger

(c) Displacement of plunger

Fig.15 Plunger motion characteristics in different diameter of plunger

（4）**The effect of nozzle diameter**

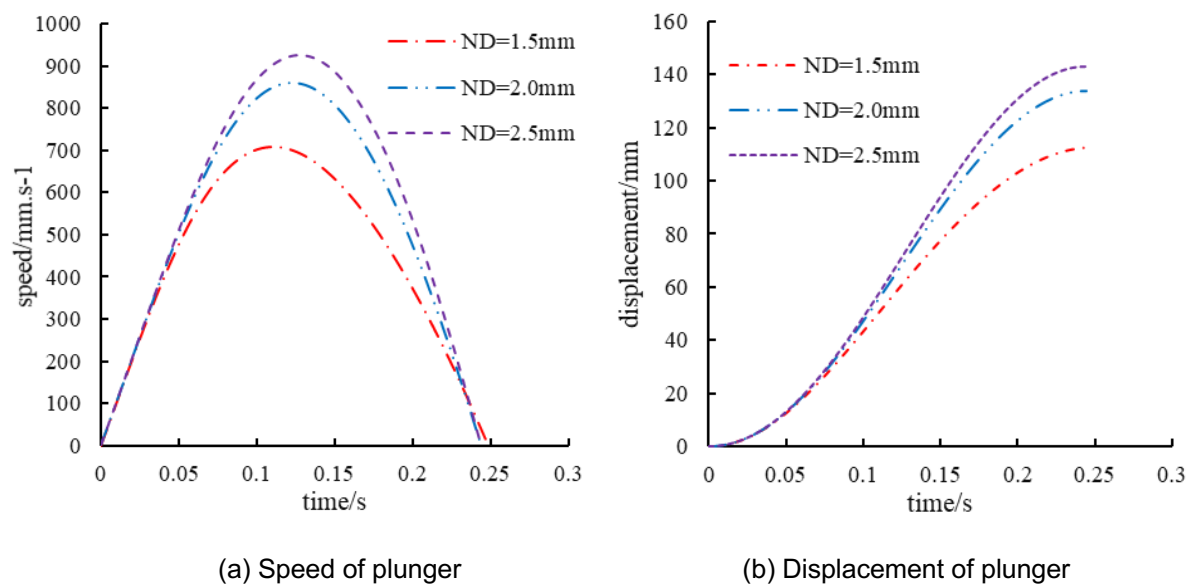(a) Speed of plunger

(b) Displacement of plunger

Fig.16 Plunger motion characteristics in different frequency

Fig.16 plots the distribution of speed and displacement of plunger with different nozzle diameter. It is worth noting that with increasing the diameter of nozzle, the speed and displacement of the plunger tends to increase. Before 0.07 s, the diameter of the nozzle has little effect on the velocity and displacement of the plunger. However, after 0.07 s, with increasing the diameter of the nozzle, the velocity and displacement of the plunger increase slowly, because the increase of the plunger makes the internal pressure increase and counteract part of WOB, thus reducing the acceleration of the plunger. In terms of displacement, the increase in nozzle diameter increases the stroke of the plunger

2.3.4 Distribution of impinging pressure with time

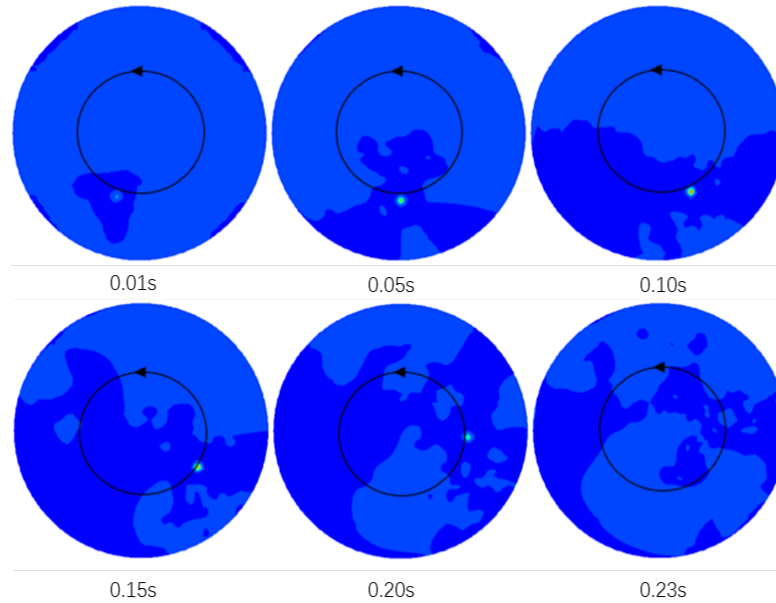|		
0.01s	0.05s	0.10s
0.15s	0.20s	0.23s

Fig.17 Distribution of impinging pressure with time

Fig.17 shows the impinging pressure over time at the bottom of a well. It is observed that the impinging pressure has a tendency to increase at first and then decrease with time, the reason for this phenomenon is that, at the beginning of the plunger movement, the plunger moves slowly and the pressure of the fluid in the chamber is small, the velocity of the jet at the exit of nozzle is small; with the increase of the plunger velocity, the jet velocity gradually increases, so that the impinging pressure gradually increases; when the resultant force provided by the spring force and liquid pressure exceeds the WOB, the speed of the plunger decreases，and the jet velocity decreases too, resulting in a decrease in the impinging pressure. Because the bit rotates at a rate of 92 r/min at the bottom hole, the pressurization period is 0.23 s, so the angle of rotation of the jet is 127° for each pressurisation cycle/pulse.

2.3.5 Impinging pressure with stand-off distance

To better demonstrate the impinging pressure with time, the distributions of impinging pressure with stand-off distance are investigated in Fig.18. It is found that the maximum impinging pressure is at the centre of the jet, and the impinging pressure decreases with the increase of the radial distance. It is worth noting that when the radial distance is less than 2 mm, the impinging pressure decays quickly with the increase of the radial distance; when the radial distance is greater than 2 mm, the impinging pressure decays slowly; when the radial distance is 4 mm, the impinging pressure decreases to 0 MPa.

(a) 0.05s   (b) 0.10s

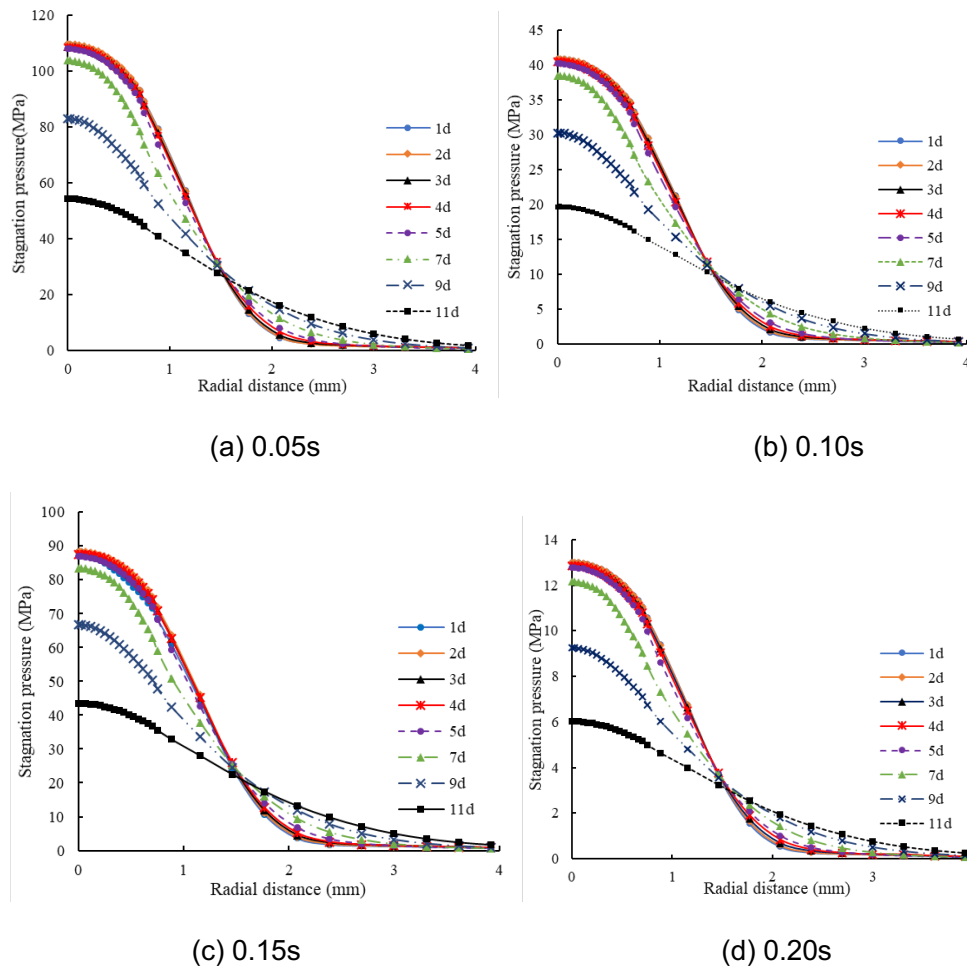(c) 0.15s   (d) 0.20s

Fig.18 Characteristics of impinging pressure with different stand-off distance at different stages of the dynamic pressure pulse

The radial distribution characteristics of the impinging pressure are basically the same when the injection distance is less than 7 times the diameter of nozzle. The main reason for this phenomenon is that when the jet is formed, the potential core of the jet is stable at 7 times the diameter of the nozzle, where the velocity of the jet is equal to the velocity at the nozzle exit, and the velocity distribution characteristics are consistent, resulting in the consistent distribution of impinging pressure. When the axial distance is greater than 7 times the diameter of the nozzle, the impinging pressure at the centre of the jet decays quickly, the main reason for this phenomenon is that in the process of advance, the jet continues to entrap the surrounding liquid and diffuse to the surroundings, resulting in energy loss, which leads to velocity attenuation along the axial direction, therefore, the impinging pressure is gradually reduced. To improve the ability of rock breaking by water jet, the stand-off distance should be less than 7 times the diameter of nozzle.

2.4 Discussion

It was confirmed by Drillstar that the percussive mud-hammer's effective operational range uses a small WOB and high frequency (Fig. 19) and that this will yield insufficient energy to activate a vibrational intensifier that could produce the targeted 150 MPa. Intensifier design has switched to

focus on other technologies (such as screw type intensifiers).
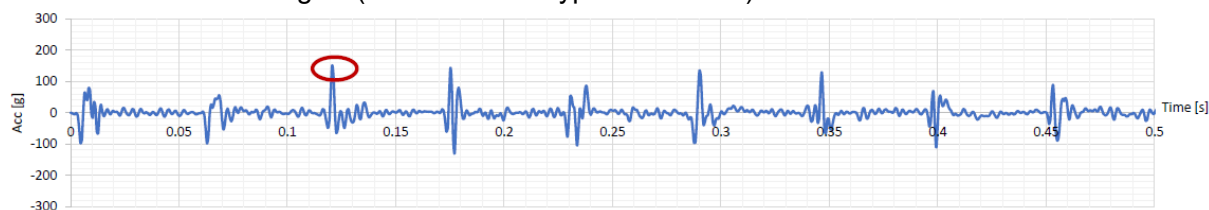

Fig.19 Mud hammer vibration frequency

3 Numerical simulation of nozzle with different chamber pressure

3.1 Task description

3.1.1 Description of velocity model

ORCHYD Partner ICL is to develop the HPWJ-rock destruction model for which they require velocity profiles of jets as they leave the nozzle orifice, for a range of chamber pressures. ICL simulation results can then be compared with laboratory jetting experiments performed with a specific nozzle, as used by partner ARMINES and reported elsewhere in WP5.

Task 1 is to provide ICL with velocity profiles for (i) at the far-left nozzle end and (ii) at 1 mm from the orifice outlet. The nozzle orifice diameter is 1 mm, and the fluid viscosity and density taken to be that for 20 degrees C pure clean water. The quasi-steady chamber pressure is set to a series of high values of interest: 100 MPa,160 MPa, 205 MPa, 250 MPa.
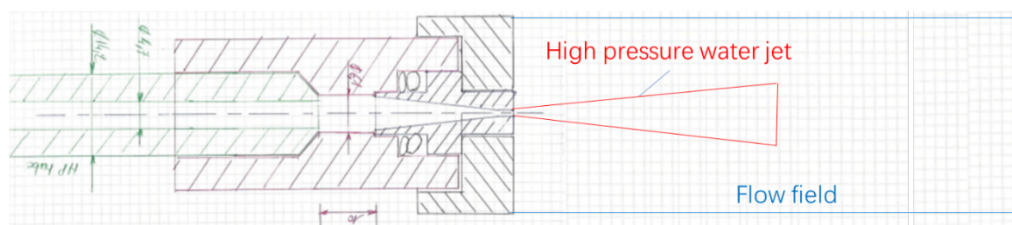

Fig.20 Schematic diagram of velocity model

3.1.2 Description of impinging pressure model

Task 2: For a constant pressurizing chamber pressure of 100 MPa,160 MPa, 205 MPa, 250 MPa, (achievable in laboratory and optimistic for field test), using exact Karcher 1 mm nozzle details as provided in attached drawings and described above: Note that the wall region (yellow/ green/black region in figure 21) defines a no inflow/outflow domain boundary, and the light blue region /red region at the left figure shows the fluid flow domain has a large outflow area given by the 14.5 mm wide annulus, and outflow boundary condition is with a zero pressure condition imposed. The centre of the figure is the inlet with a diameter of 1 mm. Impinging pressure distributions at boundary plate set at stand-off distance 3 mm, 6 mm and 10 mm.
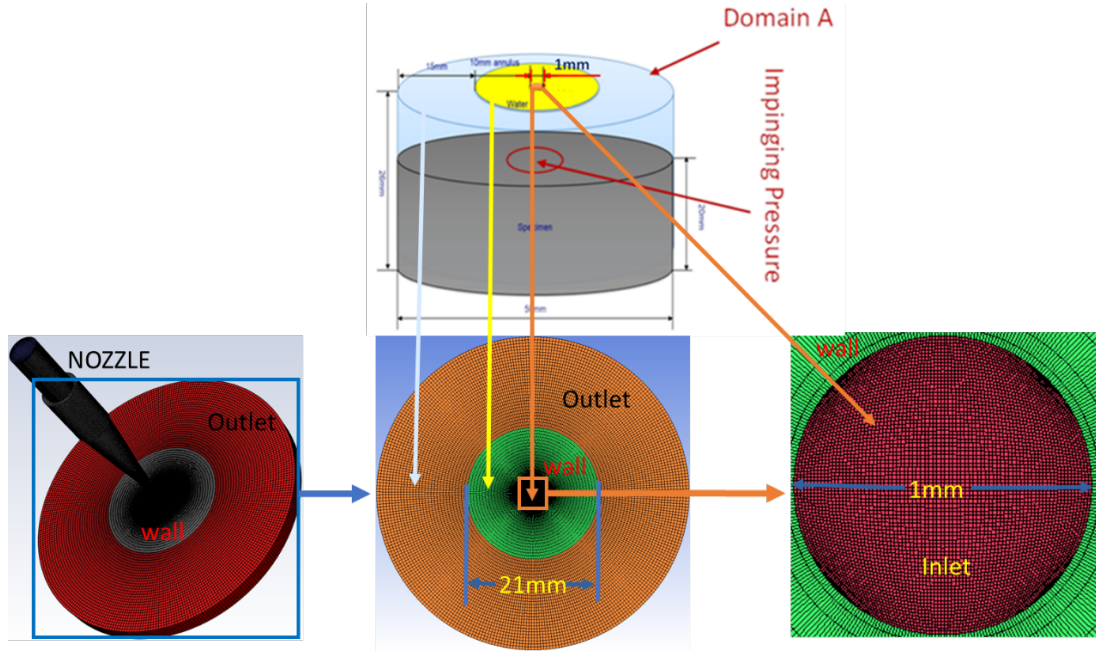
Fig.21 Schematic diagram of impinging pressure model

3.2 Method of numerical simulation

Based on the nozzle structure provided by ICL, the flow field of nozzle is established. The quasi-steady chamber pressure is set to 100 MPa,160 MPa, 205 MPa, 250 MPa respectively. The turbulent flow is described by RNG k-ε. A "pressure-inlet boundary" condition is used at the entrance to the nozzle, and this pressure is the gauge pressure. Note that the outlet boundary condition is with a zero-pressure condition). The liquid in the pressurized chamber is pure water. We also apply the incompressible flow assumption, assuming a pure water dynamic viscosity and density for 20 degrees C.

In order to verify the influence of turbulence model on water jet, numerical simulation of RNG k-ε, standard k-ε and realizable k-ε is carried out respectively. The governing equations for these three turbulence models are as follows:

RNG k-ε

$$\begin{cases} \dfrac{\partial}{\partial t}(\rho k) + \dfrac{\partial}{\partial x_i}(\rho k u_i) = \dfrac{\partial}{\partial x_j}\left[\left(\mu + \dfrac{\mu_t}{\sigma_k}\right)\dfrac{\partial k}{\partial x_j}\right] + P_k - \rho\varepsilon \\[4mm] \dfrac{\partial}{\partial t}(\rho\varepsilon) + \dfrac{\partial}{\partial x_i}(\rho\varepsilon u_i) = \dfrac{\partial}{\partial x_j}\left[\left(\mu + \dfrac{\mu_t}{\sigma_\varepsilon}\right)\dfrac{\partial\varepsilon}{\partial x_j}\right] + C_{1\varepsilon}\dfrac{\varepsilon}{k}P_k - C_{2\varepsilon}^*\rho\dfrac{\varepsilon^2}{k} \end{cases} \tag{5}$$

$$C_{2\varepsilon}^* = C_{2\varepsilon} + \frac{C_\mu\eta^3(1-\eta/\eta_0)}{1+\beta\eta^3}, \ \eta = \frac{Sk}{\varepsilon} = \frac{\left(2S_{ij}^2\right)^{1/2}k}{\varepsilon}$$

Realizable k-ε

$$\frac{\partial(\rho k)}{\partial t} + \frac{\partial(\rho k u_i)}{\partial x_i} = \frac{\partial}{\partial x_j}\left[\left(\mu + \frac{\mu_t}{\sigma_k}\right)\frac{\partial k}{\partial x_j}\right] + G_k + G_b - \rho\varepsilon - Y_M \tag{6}$$

$$\frac{\partial(\rho k)}{\partial t}+\frac{\partial(\rho k u_i)}{\partial x_i}=\frac{\partial}{\partial x_j}\left[\left(\mu+\frac{\mu_t}{\sigma_k}\right)\frac{\partial k}{\partial x_j}\right]+G_k+G_b-\rho\varepsilon-Y_M+S_\varepsilon \quad (7)$$

$$\frac{\partial(\rho\varepsilon)}{\partial t}+\frac{\partial(\rho\varepsilon u_i)}{\partial x_i}=\frac{\partial}{\partial x_j}\left[\left(\mu+\frac{\mu_t}{\sigma_\varepsilon}\right)\frac{\partial\varepsilon}{\partial x_j}\right]+\rho C_1 S_\varepsilon-\rho C_2\frac{\varepsilon^2}{k+\sqrt{v\varepsilon}}+C_{1\varepsilon}\frac{\varepsilon}{k}C_{3\varepsilon}G_b+S_\varepsilon \quad (8)$$

Where

$$C1=\max\left(0.43,\frac{\eta}{\eta+5}\right)$$

$$\eta=\left(2E_i\cdot E_i\right)^{1/2}\frac{k}{\varepsilon}$$

$$E_{ij}=\frac{1}{2}\left(\frac{\partial u_i}{\partial x_j}+\frac{\partial u_j}{\partial x_i}\right)$$

$$\mu_t=\rho C_\mu\frac{k^2}{\varepsilon}$$

$$C_\mu=\frac{1}{A_0+A_s U^* k/\varepsilon}$$

Standard **k-ε**

$$\frac{\partial}{\partial t}(\rho k)+\frac{\partial}{\partial x_i}(\rho k\mu_i)=\frac{\partial}{\partial x_j}\left[\left(\mu+\frac{\mu_i}{\sigma_k}\right)\frac{\partial k}{\partial x_i}\right]+G_k+G_b-\rho\varepsilon-Y_m+S_k$$

$$\frac{\partial}{\partial t}(\rho\varepsilon)+\frac{\partial}{\partial x_j}(\rho k\mu_i)=\frac{\partial}{\partial x_j}\left[\left(\mu+\frac{\mu_i}{\sigma\varepsilon}\right)\frac{\partial\varepsilon}{\partial x_j}\right]+G_{1\varepsilon}\frac{\varepsilon}{k}\left(G_k+C3\varepsilon Gb\right)_b-C_2\rho\varepsilon\frac{\varepsilon^2}{k}+S_\varepsilon-R_\varepsilon$$

$$(9)$$

3.3 The establishment of numerical simulation model

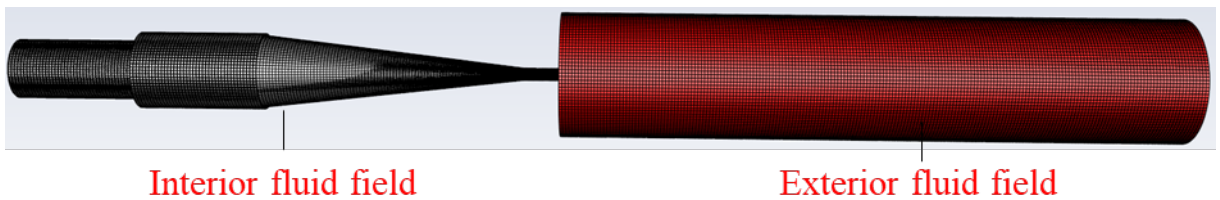### 3.3.1 Velocity distribution model

Fig.22 Velocity distribution model

To study the effect of the pressure on the water jet, the flow field inside the nozzle is established. The velocity distribution model of the nozzle is shown in figure 22, the model capturing the nozzle and jet response contains the interior fluid field and exterior fluid field.

3.4 Impinging pressure model

According to the requirements of the ICL cases of interest, the stand-off distance is set to 3 mm, 6 mm and 10 mm respectively. The quasi-steady chamber pressure is set to 100 MPa,160 MPa, 205 MPa, 250 MPa respectively. Note that the pressure generated from an intensifier pulsates over a certain period. The Impinging pressure model is shown in figure 23.
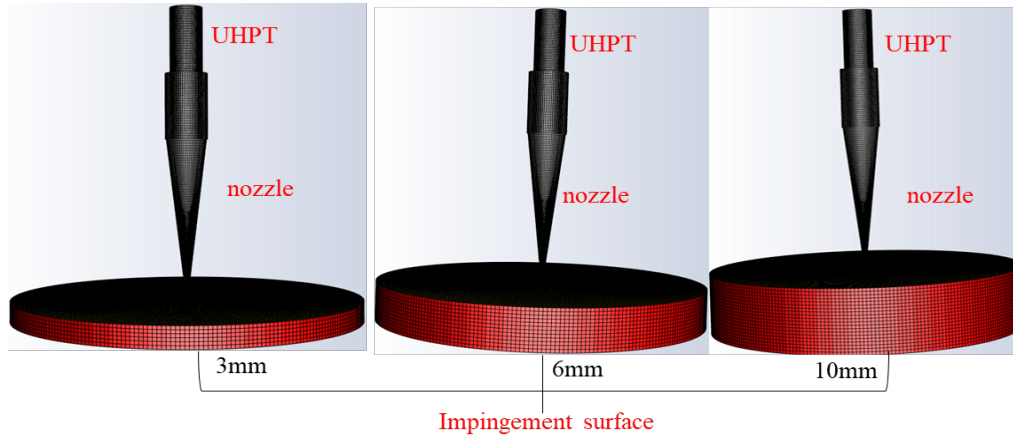

Fig.23 Impinging pressure model

3.5 Results and discussion

3.5.1 Influence of turbulence model on water jet

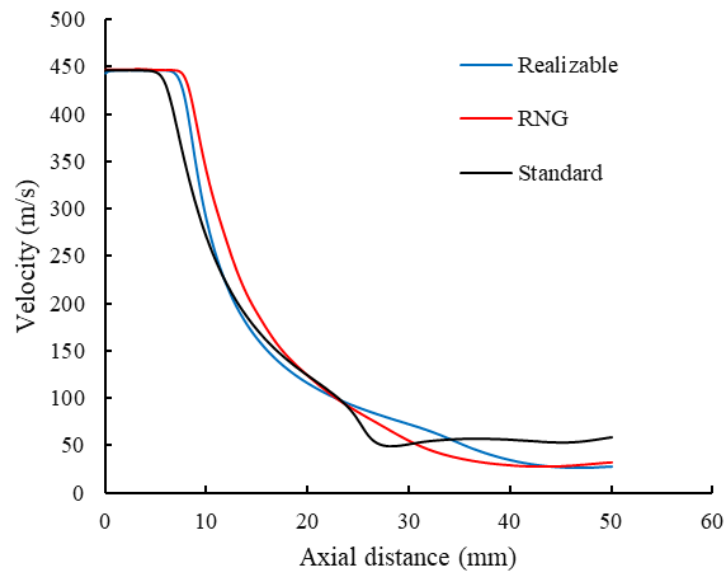**(1) Velocity** along axial distance with different turbulence model

Fig.24 Velocity along axial distance with different turbulence model

Fig.24 compares the velocity distributions with different turbulence models along the axial direction. The velocity of the three models at the orifice outlet is basically the same, but with the increase of the axial distance, the velocity changes significantly. The standard k-ε model has the smallest potential core, the length of potential core is about 4 mm. The potential core of Realizable model and RNG k-ε model is basically the same, and the length of potential core is about 7 mm. With the further increase of axial distance, the velocity

attenuation of standard k-ε turbulence model is more rapid. The velocity attenuation of standard k-ε turbulence model is the slowest. The RNG k-ε model is used as the turbulence model for jet simulation because of its higher simulation accuracy.

(2) Impinging pressure with different turbulence models

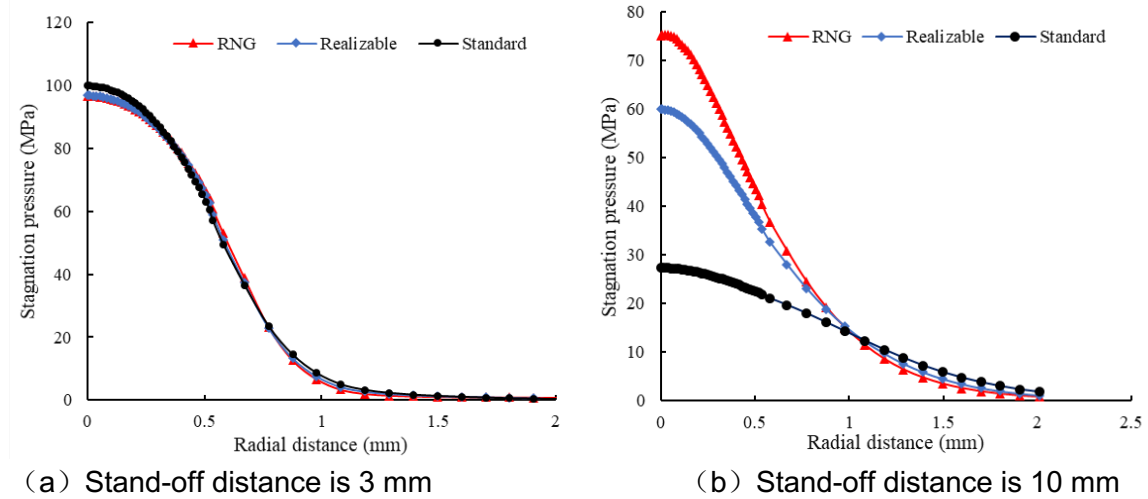（a）Stand-off distance is 3 mm　　　　　　（b）Stand-off distance is 10 mm

Fig.25 Impinging pressure with different turbulence models

Fig.25 shows the impinging pressure with different turbulence model. When the stand-off distance is 3 mm, the impinging pressure of the three models are basically the same. As the radial distance increases, the impinging pressure decreases gradually, and when the radial distance is 1.5 mm, the impinging pressure decays to 0 MPa. And when the stand-off distance is 10 mm, there are great differences in the distribution of impinging pressure. The RNG model has the maximum impinging pressure, while the standard model has the minimum, this is consistent with the attenuation characteristics of velocity.
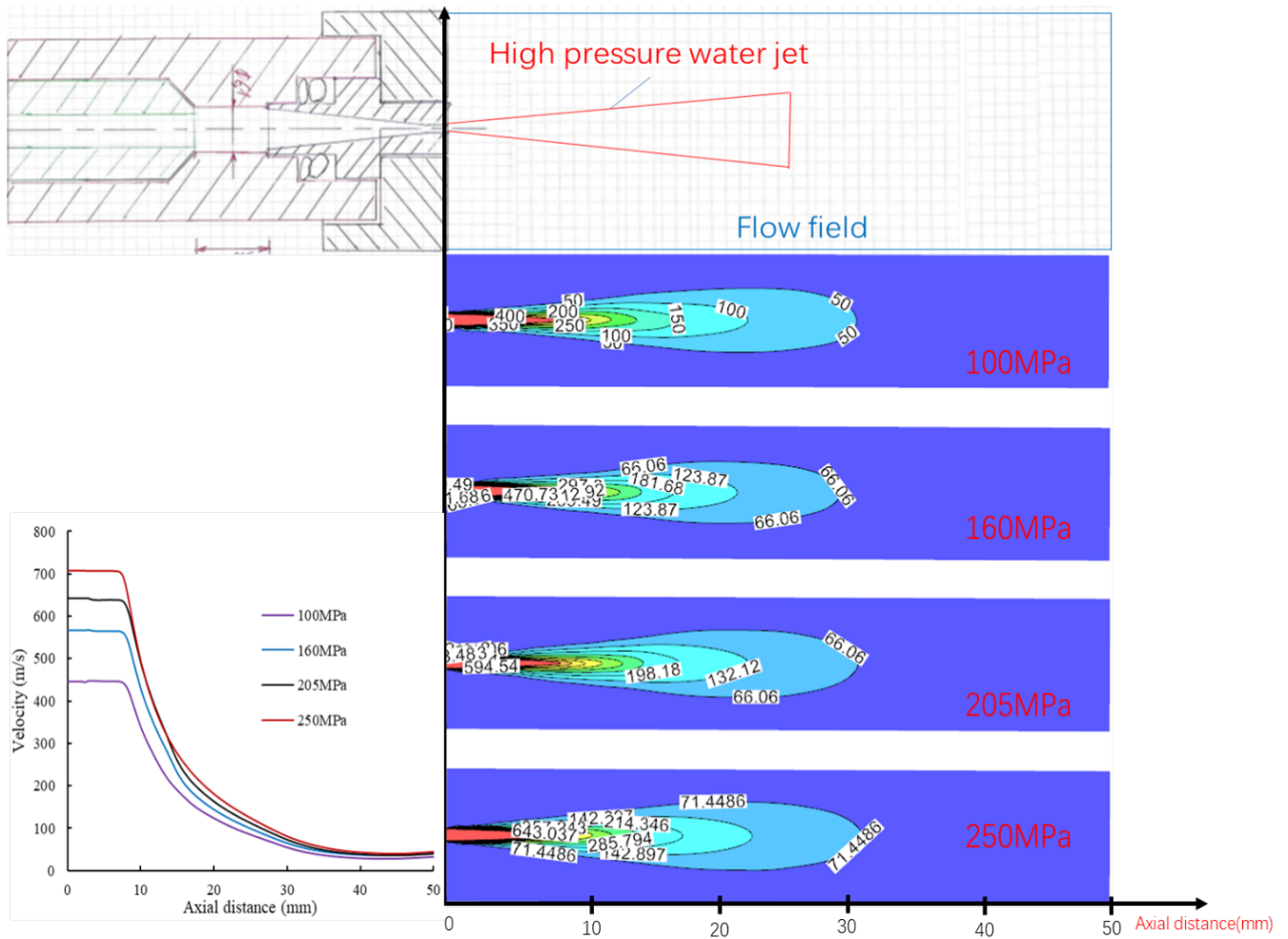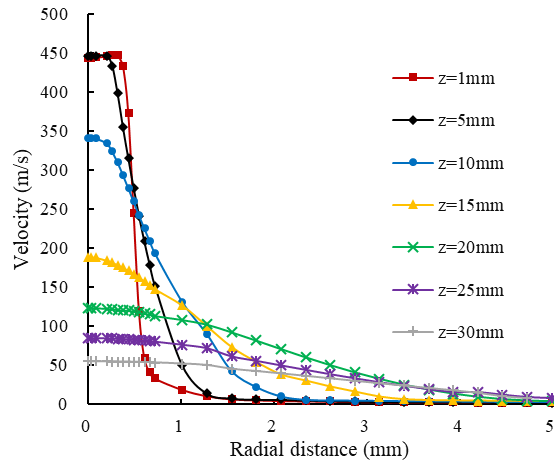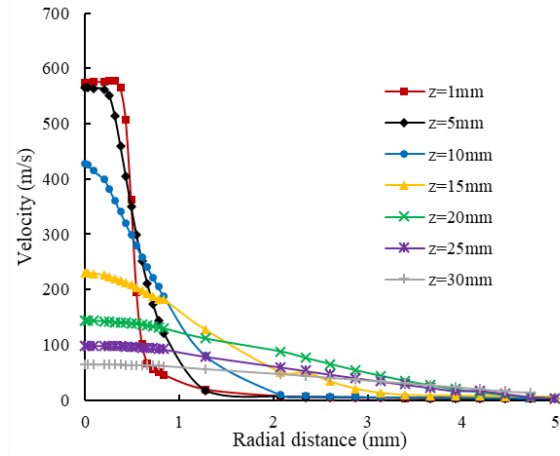
3.5.2 Velocity distribution of nozzle

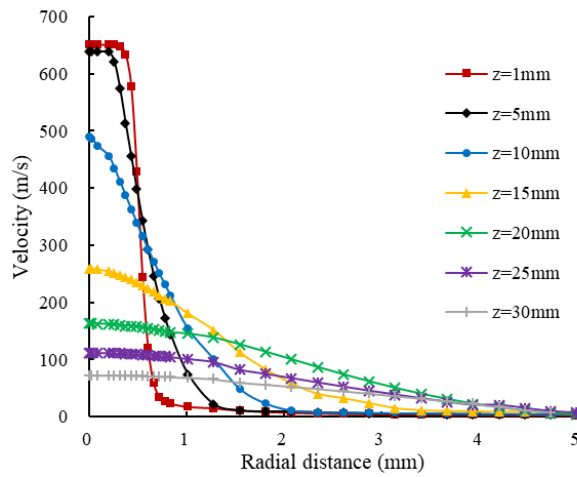Fig.26 Velocity distribution along axial direction

As we can see from figure 26, with the increase of inlet pressure, the outlet velocity increases. The velocity at 1 mm orifice outlet is 446 m/s (100 MPa), 567 m/s (160 MPa), 643 m/s (205 MPa) and 706 m/s (250 MPa) respectively, the velocity at an axial distance of 10 mm from the nozzle exit decays as 338 m/s (100 MPa), 443 (160MPa), 506 m/s (205 MPa) and 511 m/s (250 MPa) respectively, they are very different. Length of the potential core (7 mm) is about 7 times the diameter of the nozzle. In the potential core region (distance is 0 mm to 7 mm), the velocity is basically stable, and gradually decreases with the increase of axial distance. In addition, the rate of decay is constantly decreasing with the increasing of distance.
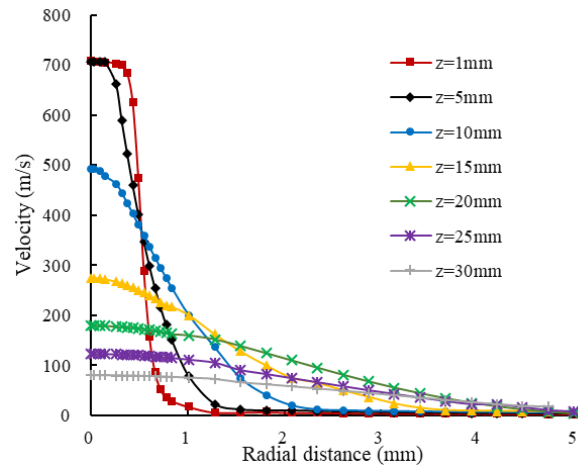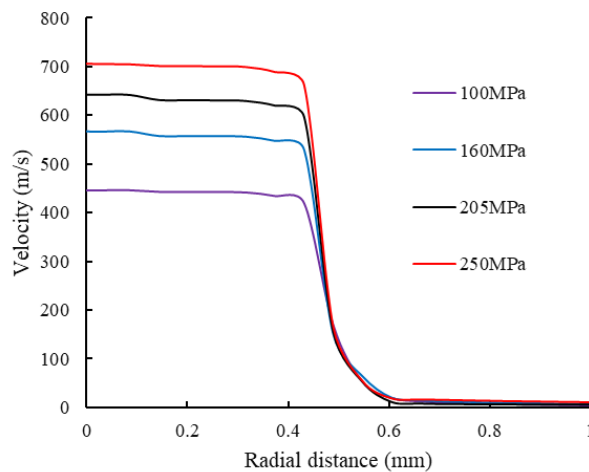
(a) 100 MPa

(b) 160 MPa

(c) 205 MPa

(d) 250 MPa

(e) velocity at Z = 0 mm, summary for all chamber pressure cases

Fig.27 Velocity distribution along radial direction

Figure 27 shows the velocity distribution at radial distances from the jet axis for different chamber pressures and for a series of distances, z from the orifice. As we can see from this figure, the maximum velocity is located at the axis, and the velocity decreases rapidly with the increase of radial distance. Within a distance of 5 mm, the velocity distribution along the radial direction is roughly constant, and with the increase of the radial distance, the velocity decreases sharply marking the margin of the 'top-hat' shaped jet core. When the axial distance is more than 5 times the diameter of nozzle, with the increase of axial distance, the rate of velocity decay decreases gradually along radial direction. The increase of inlet pressure increases the velocity but does not change the radial distribution of the velocity.
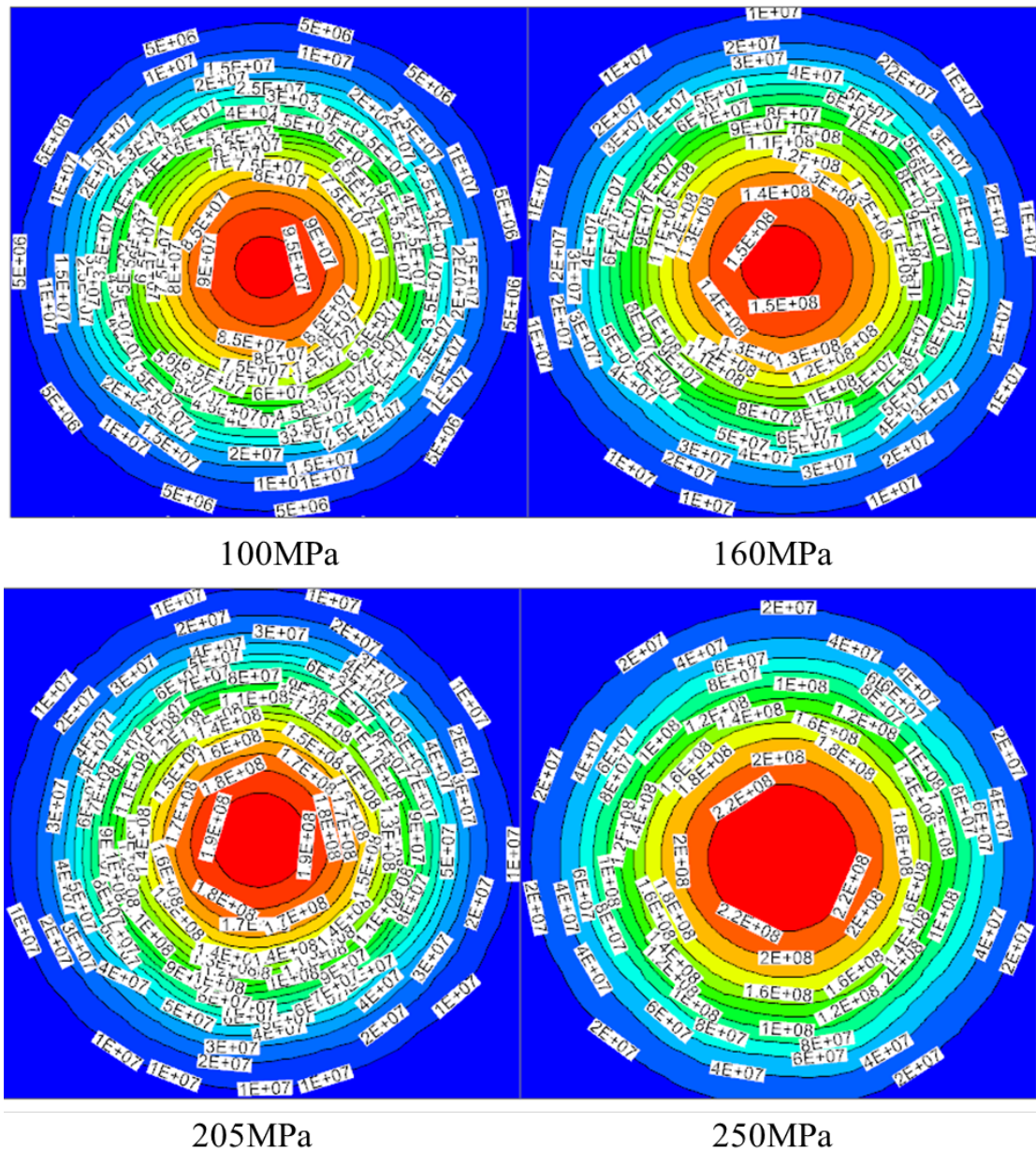
3.5.3 Impinging pressure

Fig.28 Contour of impinging pressure at different inlet pressure (stand-off distance is 3 mm)

Fig.28 and Fig.29 shows the impinging pressure of the nozzle with different stand-off distance. According to the requirements, the stand-off distance is set to 3mm, 6mm and 10 mm. As we

can see from this figure (Figure 29), the stand-off distance is set to 3 mm. As the inlet pressure increases, the pressure at the centre of the impingement surface increases gradually, impinging pressure at the centre of the impingement surface is about 97 MPa (100MPa), 154 MPa (160MPa),198MPa (205MPa) and 241MPa (250MPa) respectively.

Figure 29 shows the impinging pressure at different inlet pressure. The impinging pressure increases with the increase of the inlet pressure. The maximum impinging pressure is located in the centre of impingement surface, and the impinging pressure decreases rapidly with the increase of the radial distance. When the radial distance is more than 2 mm, the impinging pressure gradually decreases to 0 MPa.
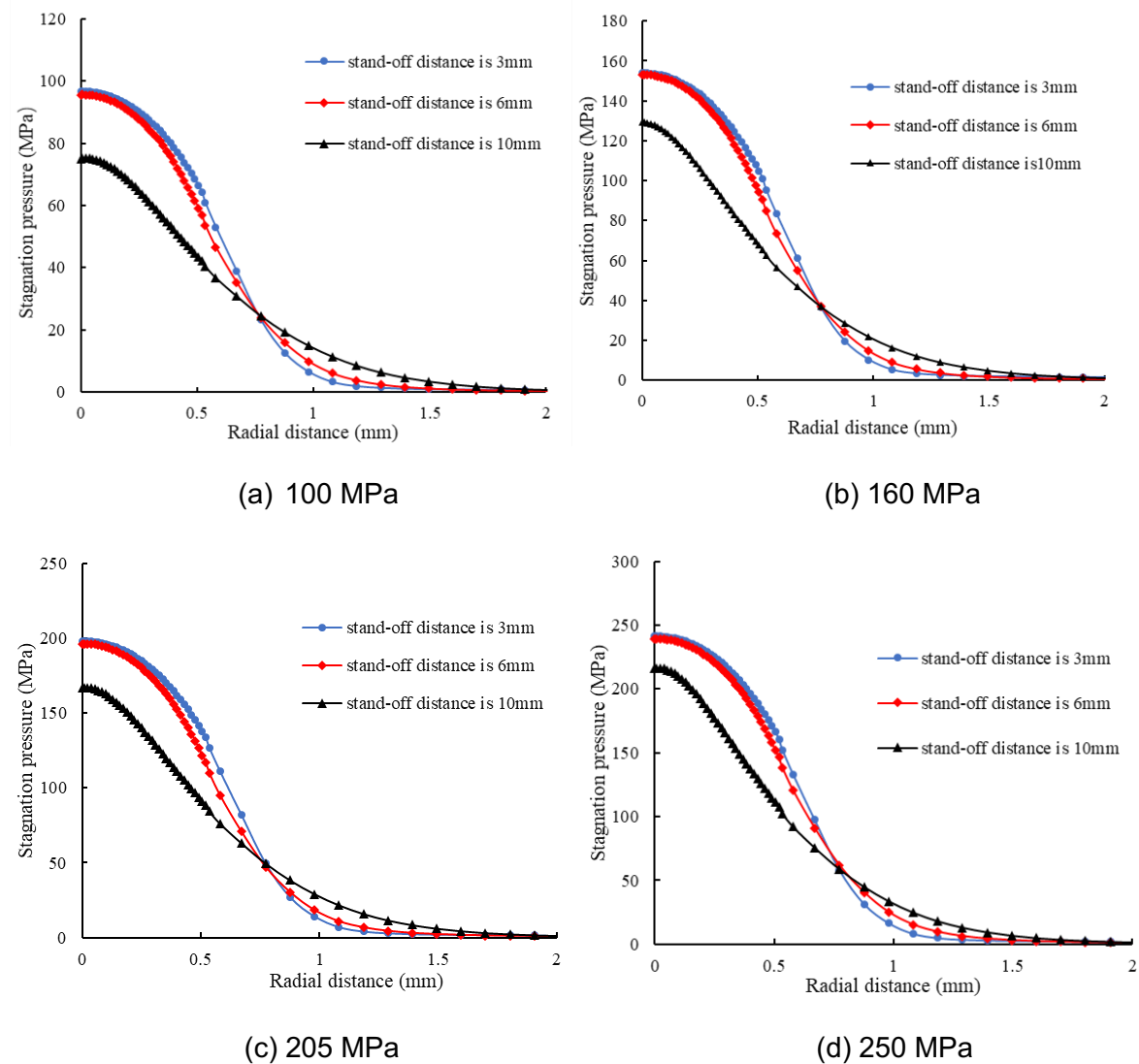

(a) 100 MPa

(b) 160 MPa

(c) 205 MPa

(d) 250 MPa

Fig.29 characteristic of impinging pressure along radial direction

4 Conclusions

1. During each piston stroke driven by the axial vibration, there are three representative stages, which are: an unstable potential core, a stable potential core, and a disappearance of potential core. In the stage of stable potential core, the change of inlet pressure does not affect the length of potential core, and the length of the potential core of jet is about 7 times the diameter

of the nozzle. When the distance is more than 7*d*, the jet continues to entrap the surrounding liquid and diffuse to the surrounding, resulting in rapid velocity decrease.

2. Increasing the plunger diameter prolongs the holding time of the high-pressure water jet, and increases the peak pressure, but it does not affect the pressurization period which is mainly influenced by the spring. When the natural frequency and axial vibration frequency of the intensifier are similar, the pressurizing capability is better; the decrease of spring stiffness is beneficial to the increase of pressure, but too small a spring stiffness increases the stroke and can cause the collapse of the spring.

3. Not surprisingly, the impinging pressure tends to increase first and then decrease with time since the pressure in the chamber operates on a dynamic cycle and the maximum impinging pressure is at the centre of the jet. When the radial distance is greater than 1.5 mm, the impinging pressure decays sharply with the increase of the radial distance. The radial distribution characteristics of the impinging pressure are basically the same and stays at a higher value when the stand-off distance is less than 7d. To improve the ability of rock breaking by water jet, the stand-off distance should be less than 7d.

4. The standard k-ε model simulates the smallest potential core, the length of potential core is about 4 mm. The potential core simulation of Realizable k-ε model and RNG k-ε model is basically the same, and the length of potential core is about 7 mm. With the further increase of axial distance, the velocity attenuation of standard k-ε turbulence model is more rapid. The velocity attenuation of standard k-ε turbulence model is the slowest. The RNG k-ε model is used as the turbulence model for jet simulation because of its higher simulation accuracy.

5. With the increase of inlet pressure, the velocity of outlet increases, the velocity at 1 mm orifice outlet is 456 m/s (100 MPa), 567 m/s (160 MPa), 643 m/s (205 MPa) and 706 m/s (250 MPa) respectively, but the velocity at 10 mm from the nozzle outlet decays as 338 m/s (100 MPa), 443 (160 MPa), 506 m/s (205 MPa) and 511 m/s (250 MPa) respectively. Length of the potential core (7 mm) is about 7 times the diameter of the nozzle. In this potential core region (distance is 0 mm to 7 mm), the velocity is basically stable, and gradually decreases with the increasing of distance. In addition, the rate of decay is constantly decreasing with the increasing of distance.

6. As the inlet pressure increases, the pressure at the centre of the impingement surface increases gradually, impinging pressure at the centre of the impingement surface is about 97 MPa (100 MPa), 154 MPa (160 MPa),198 MPa (205 MPa) and 241 MPa (250 MPa) respectively. The impinging pressure increases with the increase of the inlet pressure. The maximum impinging pressure is located in the centre of Impingement surface, and the impinging pressure decreases rapidly with the increase of the radial distance. When the radial distance is more than 2 mm, the impinging pressure gradually decreases to 0 MPa.

References:

[1] Liao H, Guan Z, Shi Y., Field tests and applicability of downhole pressurized jet assisted drilling techniques. International Journal of Rock Mechanics and Mining Sciences, pp.140-146.

[2] Guan Z C, Liu Y W, Wei W Z., Downhole drill string absorption & hydraulic supercharging device working principle and analysis of speed-increasing effect. Petroleum Drilling Techniques, pp.8-13.

[3] Liu Y, Guan Z, Zhang H., A downhole high-pressure jet drilling device transforming drilling string vibration energy. Natural Gas Industry, pp.91-96.

[4] Liao H, Li G, Niu J. Influential factors and mechanism analysis of rock breakage by ultra high pressure water jet under submerged condition. Chinese Journal of Rock Mechanics and Engineering, 2008, pp.1243-1250.